NeuroImage 45 (2009) S51–S60

Contents lists available at ScienceDirect

NeuroImage

journal homepage: www.elsevier.com/locate/ynimg

Time sequence diffeomorphic metric mapping and parallel transport track time-dependent shape changes

Anqi Qiu [a,b,*], Marilyn Albert [c], Laurent Younes [d], Michael I. Miller [e]

[a] Division of Bioengineering, National University of Singapore, Singapore
[b] Singapore Institute for Clinical Sciences, the Agency for Science, Technology and Research, Singapore
[c] Department of Neurology, Johns Hopkins University School of Medicine, Baltimore, MD, USA
[d] Department of Applied Mathematics and Statistics, Johns Hopkins University, Baltimore, MD, USA
[e] Center for Imaging Science, Johns Hopkins University, Baltimore, MD, USA

ARTICLE INFO

Article history:
Received 15 October 2008
Accepted 15 October 2008
Available online 7 November 2008

Keywords:
Time sequence registration
Diffeomorphic metric mapping
Parallel transport
Longitudinal shape changes

ABSTRACT

Serial MRI human brain scans have facilitated the detection of brain development and of the earliest signs of neuropsychiatric and neurodegenerative diseases, monitoring disease progression, and resolving drug effects in clinical trials for preventing or slowing the rate of brain degeneration. To track anatomical shape changes in serial images, we introduce new point-based time sequence large deformation diffeomorphic metric mapping (TS-LDDMM) to infer the time flow of within-subject geometric shape changes that carry known observations through a period. Its Euler–Lagrange equation is generalized for anatomies whose shapes are characterized by point sets, such as landmarks, curves, and surfaces. The time-dependent momentum obtained from the TS-LDDMM encodes within-subject shape changes. For the purpose of across-subject shape comparison, we then propose a diffeomorphic analysis framework to translate within-subject deformation in a global template without incorporating across-subject anatomical variations via parallel transport technique. The analysis involves the retraction of the within-subject time-dependent momentum along the TS-LDDMM trajectory from each time to the baseline, the translation of the momentum in a global template, and the reconstruction of the TS-LDDMM trajectory starting from the global template.

Introduction

Spatial–temporal images have been widely used in the field of medical image to record function and anatomy of human organs. Serial MRI human brain scans have facilitated the detection of brain development and of the earliest signs of neuropsychiatric and neurodegenerative diseases, monitoring disease progression, and resolving drug effects in clinical trials for preventing or slowing the rate of brain degeneration (Thompson et al., 2000; Chung et al., 2001; Wang et al., 2003; Apostolova et al., 2006b; Qiu et al., 2008a,b; Xue et al., 2007). For instance, researchers have identified progressive hippocampal volume loss to be one of the hallmarks of Alzheimer's disease (AD). Using brain warping techniques, neuroimaging studies previously found that patterns of hippocampal shape change distinguished early AD from healthy aging (Wang et al., 2003; Apostolova et al., 2006b; Qiu et al., 2008a,b). Compared to volumetric assessments, rates of anatomical shape changes provide much richer information for disease discrimination (e.g. Thompson et al., 1996a; Christensen et al., 1997; Bookstein, 1997; Chung, 2001; Terriberry et al., 2005; Ashburner and Friston, 2005; Apostolova et al., 2006a; Csernansky et al., 2004; Gilmore et al., 2007; Yu et al., 2007; Qiu et al., 2008a,b). Sensitive and accurate computational techniques are needed to track within-subject shape changes in brain structures based on serial MRI scans and then compare them across clinical populations.

To assess the location and process of atrophy or growth in a brain structure requires studying within-subject time-dependent deformation through the transformation. It characterizes the changes of anatomical coordinates from the baseline to other time points. The earliest mapping of biological coordinates via landmarks was in the early 1980s and continued by Bookstein (1978, 1991, 1996, 1997) and via dense image by Bajcsy et al. (1983), Bajcsy and Kovacic (1989), Dann et al. (1989), Collins et al. (1994), Friston et al. (1995), Davatzikos (1996), Feldmar et al. (1997), Thirion (1998), Gee and Haynor (1999), Gee (1999), Ashburner et al. (2003), Avants and Gee (2004), Avants et al. (2006), Ashburner (2007), and Rao et al. (2004). As the brain mapping based on dense image is being carried on by many of groups; the mapping restricted to the cortical manifolds, including curves and surfaces, are being studied as well (Thompson et al., 1996b; Fischl et al., 1999; van Essen, 2004; Vaillant and Glaunès, 2005; Yu et al., 2007; Chung et al., 2008; Mangin et al., 2004; Collins et al., 1998; Hellier and Barillot, 2003; Cachier et al., 2001). Among these template-based brain mapping techniques, Large Deformation Diffeomorphic Metric Matching (LDDMM) algorithms have recently received a great attention. They provide a range of diffeomorphic matching methods

* Corresponding author. Division of Bioengineering, National University of Singapore, 7 Engineering Drive, 1, Block E3A 04-15, Singapore, 117574. Fax: +65 6872 3069.
E-mail address: bieqa@nus.edu.sg (A. Qiu).

1053-8119/$ – see front matter © 2008 Elsevier Inc. All rights reserved.
doi:10.1016/j.neuroimage.2008.10.039

for landmarks, curves, surfaces, images, vectors, as well as tensors (Joshi and Miller, 2000; Beg et al., 2005; Vaillant and Glaunès, 2005; Cao et al., 2005a,b; Glaunès et al., 2008; Qiu and Miller, 2007; Vaillant et al., 2007). All of these mapping algorithms provide diffeomorphic maps — one-to-one, reversible smooth transformations that preserve topology. The use of LDDMM for studying the shapes of objects implies the placement of shapes in a metric space, provides a diffeomorphic transformation, and defines a metric distance that can be used to quantify the similarity between two shapes. Moreover, LDDMM provides a mechanism that allows for the reconstitution of the variations by encoding precise variations of anatomies relative to the template. The resultant template-based representation can be interpreted as a change of coordinates, representing anatomies in a local chart centered at the template. They have been successfully applied to a variety of functional and structural MRI studies (Miller et al., 2005; Qiu et al., 2007, 2008a; Kirwan et al., 2007; Qiu and Miller, 2008; Bakker et al., 2008).

Within-subject anatomical variation in multiple time points is naturally represented by the deformation needed to pass from the anatomy at the baseline through the anatomies at the remaining time points. When comparing two or more subjects, the absence of a common coordinate system across subjects can undermine hypothesis testing related to time-dependent within-subject deformation. One approach commonly used in the previous studies is to map subjects' structures at different time points to a global template via brain warping techniques (Wang et al., 2003). The difficulty with this approach is that the transformations used to assess longitudinal changes in the structure included the variation of the transformation between different time points within and across subjects together. The weakness of this approach for detecting within-subject changes is that the variation across subjects is generally larger than the variation within subjects. The other commonly used approach is to map the anatomy at the baseline to the other time point and then translate the Jacobian determinant of the within-subject deformation to the global template by modulating the Jacobian determinant of the deformation between the subject and the global template (Kipps et al., 2005; Brambati et al., 2007). Again, across-subject deformation is involved in the group comparison. Recently, we have introduced a new technique in the LDDMM framework that decides how change in the anatomy of one subject can be translated into the similar deformation occurring in another subject without incorporating across-subject deformation in terms of remained deformation covariance structure (Younes, 2007; Younes et al., 2008; Qiu et al., 2008a,b). The metric structure on anatomies provided by LDDMM offers a consistent approach for the translation of this information. This operation, parallel translation taken from Riemannian geometry, displaces vectors along a curve without changing properties such as the norms of the vectors or their dot products. In the Euclidean space, this operation is the standard translation of vectors; i.e., the infinitesimal displacement of subject 1 is applied to subject 2 without change. In curved spaces, however, parallel translation is nonlinear. We computed by solving a differential equation. This approach with the LDDMM-surface mapping (Vaillant and Glaunès, 2005; Vaillant et al., 2007) has been used to assess the hippocampal atrophy between the baseline and followup in normal healthy controls, converters and patients with AD (Qiu et al., 2008a,b).

In this paper, we extend our previous longitudinal shape analysis (Qiu et al., 2008a,b) for tracking shape changes between two time points to multiple time points as illustrated in Fig. 1. We will first adapt the LDDMM mapping technique and develop a new algorithm, time sequence large deformation diffeomorphic metric mapping (TS-LDDMM) for constructing a trajectory connecting multiple observation of one subject in a shape space. This algorithm, which has been suggested in (Miller et al., 2002) for the image matching case, seeks the optimal time flow of geometric changes that carry the known observations through a period time. We here generalize TS-LDDMM to anatomies represented by a set of points, such as unlabeled landmarks, or curves, or surfaces. We then adapt our parallel transport strategy to time series with an analysis along the following three steps, which are applied to each subject:

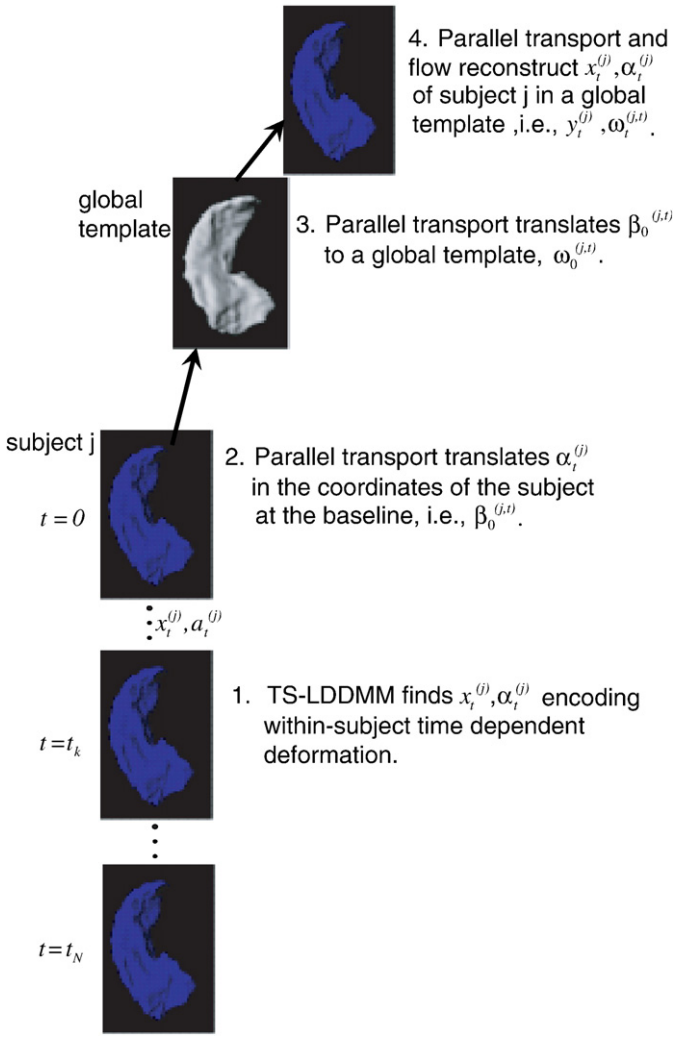

Fig. 1. A schematic for studying time dependent shape changes. $x_t^{(j)}$ is the trajectory connecting the subject j at time 0 to the one at time t. $\alpha_t^{(j)}$ is the momentum that encodes the shape change of subject j along the time.

Retraction: Parallel transport of the deformation signature along the TS-LDDMM trajectory from each time t to the baseline $t=0$.

Translation: Parallel transport the collected information from the subject baseline to a template, along a geodesic connecting the two shapes.

Extension: Reconstruct a trajectory starting from the template based on the transported information, inverting the first step.

We organize this paper by first reviewing static point-based LDDMM algorithms and then extend them to the dynamic case (Time sequence large deformation diffeomorphic metric mapping for landmarks, curves, and surfaces (TS-LDDMM)). Finally, we will describe the technique of parallel transport in diffeomorphisms.

Static point-based large deformation diffeomorphic metric mapping

In the setting of diffeomorphic metric mapping, the set of anatomical shapes are placed into a metric shape space. This is modeled

by assuming that the shape is generated one from the other via a flow of diffeomorphisms, solutions of ordinary differential equations $\dot{\phi}_t = v_t(\phi_t), t\in[0,1]$ starting from the identity map ϕ_0=id, and associated velocity vector fields v_t, $t\in$[0,1]. We define a metric distance between target shape I_{targ} and template shape I_{temp} as the length of the geodesic curves $\phi_t \cdot I_{temp}, t\in[0,1]$ through the shape space such that $\phi_1 \cdot I_{temp} = I_{targ}$ at time t=1. For instance, in the landmark case, $I_{temp}=(x_i)_{i=1}^n$ and the group action is taken as $\phi_1 \cdot I_{temp} = \phi_1(x_i)_{i=1}^n$. These geodesics $\phi_t \cdot I_{temp}, t\in[0,1]$ are generalizations of simple finite dimensional curves. The metric between two shapes I_{temp}, I_{targ} is determined by the integrated norm $||v_t||_V$ of the vector field generating the transformation, where $v_t\in V$, a smooth Hilbert space with kernel k_V and norm $||\cdot||_V$. To ensure solutions are diffeomorphisms, V must be a space of smooth vector fields (Trouvé, 1995; Dupuis et al., 1998). Equivalently, the metric distance can be computed through m_t, termed the momentum, a linear transformation of v_t defined by the kernel, $k_V: v_t \to m_t = k_V^{-1} v_t$ according to

$$\begin{aligned}\rho(I_{temp}, I_{targ})^2 &= \inf_{v_t:\dot{\phi}_t = v_t(\phi_t), \phi_0 = id} \int_0^1 ||v_t||_V^2 dt \\ &\quad \text{such that } \phi_1 \cdot I_{temp} = I_{targ} \\ &= \inf_{m_t:\dot{\phi}_t = k_V m_t(\phi_t), \phi_0 = id} \int_0^1 \langle m_t, k_V m_t \rangle_2 dt \\ &\quad \text{such that } \phi_1 \cdot I_{temp} = I_{targ}.\end{aligned} \tag{1}$$

The Euler equation associated to Eq. (1) indicates that the momentum m_t along the geodesic ϕ_t is conserved (Miller et al., 2002, 2006) (it is constant when expressed in a fixed coordinate system). This implies that the initial momentum m_0 encodes the geodesic connecting I_{temp} and I_{targ}, the conservation equation being

$$\frac{dm_t}{dt} + \mathbf{D}v_t m_t + m_t \nabla \cdot v_t + \mathbf{D}m_t^T v_t = 0 \tag{2}$$

where **D** is the Jacobian matrix and $(\nabla\cdot)$ is the divergence operator. Although we wrote the equation in classical form, it must be noted that it may have singular solutions, and that this happens in particular with point-set LDDMM (the form taken by this equation for singular momenta is given below). This reduces the problem of studying shapes of a population in a nonlinear diffeomorphic metric space to a problem of studying the initial momenta in a linear space. This has been applied to landmarks and surfaces in (Vaillant et al., 2004; Qiu and Miller, 2008).

In the point-based LDDMM mapping, let $I_{temp}=\boldsymbol{x}=(x_i)_{i=1}^n$ and $I_{targ}=\boldsymbol{y}=(y_i)_{i=1}^m$ be the point sets on the objects of I_{temp} and I_{targ}, and define the trajectories $x_i(t)\doteq\phi_t(x_i)$ for i=1,..., n. The momentum, m_t, takes the singular form

$$m_t = \sum_{i=1}^n \alpha_i(t) \otimes \delta_{x_i(t)}, \tag{3}$$

where $\boldsymbol{\alpha}_i(t)$ is the momentum vector of the i^{th} point at time t. The momentum here is not a function but a discrete vector measure, the notation being interpreted by the fact that, for any smooth vector-valued function u

$$\int u(x) \cdot dm_t(x) = \sum_{i=1}^N \alpha_i(t) \cdot u(x_i(t)).$$

Let $\boldsymbol{\alpha_t}=(\alpha_i(t))_{i=1}^n$. We can rewrite Eq. (1) as

$$\begin{aligned}\rho(\boldsymbol{x},\boldsymbol{y})^2 &= \inf_{\alpha_t:\dot{\phi}_t = k_V\alpha_t, \phi_0 = id} \int_0^1 \sum_{i=1}^n \sum_{j=1}^n \left[k_V(x_i(t), x_j(t))\alpha_i(t)\right] \cdot \alpha_j(t) dt \\ &\quad \text{such that } \phi_1 \cdot \boldsymbol{x} = \boldsymbol{y}.\end{aligned} \tag{4}$$

In practice, we often introduce a matching functional, $E(\phi_1 \cdot \boldsymbol{x}, \boldsymbol{y})$, and define an inexact matching problem: find a diffeomorphism ϕ_t between two objects $\boldsymbol{x}$ and $\boldsymbol{y}$ as a minimizer of

$$\begin{aligned}J(\alpha_t) = \operatorname*{argmin}_{\alpha_t} &\int_0^1 \sum_{i=1}^n \sum_{j=1}^n \left[k_V(x_i(t), x_j(t))\alpha_j(t)\right] \\ &\cdot \alpha_i(t) dt + E(\phi_1 \cdot x, y).\end{aligned} \tag{5}$$

The matching functional, E, depends only on the positions of the finite number of points $(\phi_1(x_i))_{i=1}^n$. Here, we particularly review E when objects $\boldsymbol{x}$ and $\boldsymbol{y}$ are unlabeled points, including unlabeled landmarks, curves, and surfaces. They will be represented as discrete measures, in the form (using the same notation as above) (Glaunès et al., 2004, 2008; Vaillant and Glaunès, 2005; Qiu and Miller, 2007)

$$\mu_{\boldsymbol{x}} = \sum_i w_{x_i} \otimes \delta_{x_i}. \tag{6}$$

The action of ϕ_1 on the discrete measure $\mu_{\boldsymbol{x}}$ is given in the form of

$$\phi_1 \cdot \mu_{\boldsymbol{x}} = \sum_i w_{\phi_1(x_i)} \otimes \delta_{\phi_1(x_i)}.$$

For unlabeled landmarks, the weights, w_{x_i} are scalars; for 3D curves and surfaces, they are 3D vectors.

We use a kernel norm to compare $\phi_1 \cdot \mu_{\boldsymbol{x}}$ and $\mu_{\boldsymbol{y}}$. Let k_W be a kernel and μ be a measure. We define

$$||\mu||_{k_W}^2 \doteq \int k_w(x,y) d\mu(x) \cdot d\mu(y).$$

The W in the notation comes from the fact that k_W can be interpreted as the reproducing kernel of a vector space (W) of smooth vector-valued functions and $||\cdot||_{k_W}$ is then the dual norm (Glaunès et al., 2004, 2008; Vaillant and Glaunès, 2005; Durrleman et al., 2007; Qiu and Miller, 2007).

We will let

$$E(\phi_1 \cdot \boldsymbol{x}, \boldsymbol{y}) = ||\phi_1 \cdot \mu_{\boldsymbol{x}} - \mu_{\boldsymbol{y}}||_{k_W}^2. \tag{7}$$

With $\mu_{\boldsymbol{x}} = \sum_{i=1}^n w_{x_i} \otimes \delta_{x_i}$ and $\mu_{\boldsymbol{y}} = \sum_{j=1}^m \tilde{w}_{y_j} \otimes \delta_{y_j}$, this is equal to

$$\begin{aligned}E(\phi_1 \cdot x, y) = &\sum_{i=1}^n \sum_{j=1}^n w_{\phi_1(x_i)} \cdot w_{\phi_1(x_j)} k_W(\phi_1(x_i), \phi_1(x_j)) \\ &-2 \sum_{i=1}^n \sum_{j=1}^m w_{\phi_1(x_i)} \cdot \tilde{w}_{y_j} k_W(\phi_1(x_i), y_j) \\ &+ \sum_{i=1}^m \sum_{j=1}^m \tilde{w}_{y_i} \cdot \tilde{w}_{y_j} k_W(y_i, y_j).\end{aligned} \tag{8}$$

We now describe how this representation is implemented with unlabeled landmarks, curves and surfaces.

Unlabeled landmarks

If $\boldsymbol{x}$ and $\boldsymbol{y}$ above represent unstructured unlabeled landmarks, the weight w_{x_i} and $\tilde{w}_{y_j}$ are scalars. They can be chosen in function of the application, the simplest choices being either $w_{x_i} \equiv 1$ or $w_{x_i} \equiv 1/n$ and similarly for $\tilde{w}_{y_j}$.

Curves

When each curve is represented by a sequence of points, still denoted as $\boldsymbol{x}=(x_i)_{i=1}^n$ and $\boldsymbol{y}=(y_j)_{j=1}^m$. However, a curve cannot be uniquely reconstructed based on the locations of a set of points. We assume a curve embedded in R^3 is a one-dimensional manifold in the sense that the local region of every point on the curve is equivalent to a line which can be uniquely defined by this point and the tangent

vector at this location. We use the representation (Glaunès et al., 2008; Qiu and Miller, 2007)

$$\mu_{\boldsymbol{x}} = \sum_{i=1}^{n-1} w_{c_i} \otimes \delta_{c_i}$$

with $c_i = (x_{i+1} + x_i)/2$ and $w_{c_i} = x_{i+1} - x_i$, and similarly for $\boldsymbol{y}$. The action of ϕ_1 on c_i is approximated as $\phi_1(c_i) = (\phi_1(x_{i+1}) + \phi_1(x_i))/2$, and its corresponding $w_{\phi_1(c_i)}$ is approximated by $\phi_1(x_{i+1}) - \phi_1(x_i)$. This representation in terms of vector measure accounts for the geometry of the curve (while the scalar measure used above would treat the sequence as an unordered list of points).

Surfaces

Now, let I_{temp} and I_{targ} be triangulated meshes with vertices $\boldsymbol{x} = (x_i)_{i=1}^n$ and $\boldsymbol{y} = (y_j)_{j=1}^m$, respectively. We assume the cortical surfaces embedded in $\mathcal{R}^3$ to be a two-dimensional manifold in the sense that the neighborhood of every point on the surface is equivalent to a two-dimensional plane in Euclidean space. Such a plane can be uniquely defined by a point and a vector originated at this point and normal to the plane. We thus let (Vaillant and Glaunès, 2005; Vaillant et al., 2007)

$$\mu_{\boldsymbol{x}} = \sum_{f \in \mathcal{F}\boldsymbol{x}} w_{c_f} \otimes \delta_{c_f},$$

where $\mathcal{F}_x$ is the set of faces in the triangulation, and, for a positively ordered face $f = (x_{f_1}, x_{f_2}, x_{f_3})$, $w_{c_f} = \frac{1}{2}(x_{f_1} - x_{f_2})(x_{f_3} - x_{f_1})$ and $c_f = \frac{1}{3}(x_{f_1} + x_{f_2} + x_{f_3})$; $\mu_{\boldsymbol{y}}$ is defined similarly. $\phi_1(c_f)$ and $w_{\phi_1}(c_f)$ are respectively approximated as $\phi_1(c_f) = \frac{1}{3}(\phi_1(x_{f_1}) + \phi_1(x_{f_2}) + \phi_1(x_{f_3}))$ and $w_{\phi_1}(c_f) = \frac{1}{2}(\phi_1(x_{f_1}) - \phi_1(x_{f_2}))(\phi_1(x_{f_3}) - \phi_1(x_{f_1}))$. Here again, the representation makes a direct use of the geometry of the point set as a triangulated surface. Note that the definitions of $\mu_{\boldsymbol{x}}$ in the curve and surface cases come from discretizations of mathematical objects called currents, as described in Vaillant and Glaunès (2005).

Lemma 1. *Static variational solution.* The point-based LDDMM algorithm minimizes the energy in Eq. (5), with variables $\boldsymbol{x}_t = (x_i(t))_{i=1}^n$ and $\boldsymbol{\alpha_t} = (\alpha_i(t))_{i=1}^n$ that are related via the dynamical equations

$$\frac{dx_i(t)}{dt} = \sum_{j=1}^{n} k_V(x_i(t), x_j(t))\alpha_j(t), i = 1, 2, \ldots, n \tag{9}$$

with initial condition $\boldsymbol{x}_0 = \boldsymbol{x}$. The Euler–Lagrange optimality conditions for this variational problem imply

$$\frac{d\alpha_i(t)}{dt} = -\sum_{j=1}^{n} \alpha_i(t) \cdot \alpha_j(t) \nabla_1 k_V(x_i(t), x_j(t)), \tag{10}$$

where ∇_1 denotes taking derivative of $k_V(x_i(t), x_j(t))$ with respect to its first variable.

This was proven previously (Vaillant et al., 2004). Eqs. (9) and (10) indicate that the evolution from one object to the other is uniquely determined by α_0. Since α_0 carries the same information as $\frac{d\boldsymbol{x}(t)}{dt}$ at $t = 0$ and therefore corresponds to an infinitesimal variation of $\boldsymbol{x}_0$, we shall term $\boldsymbol{\alpha}_0$ as "deformation signature" in the static point-based LDDMM. In fact, Eq. (10) is the form taken by the conservation of momentum Eq. (2) in the singular case of point momenta.

Time sequence large deformation diffeomorphic metric mapping for landmarks, curves, and surfaces (TS-LDDMM)

In the time sequence large deformation diffeomorphic metric mapping (TS-LDDMM), time sequence observations are given and the goal is to infer the time flow of geometric change that carries the known observation through the period $t \in [0, 1]$. Here flows of point sets are diffeomorphic, with t corresponding to actual real-time, and the comparison is examined by the similarity of the observables I_t, $t \in [0, 1]$ and the observable, I_0 at $t = 0$. I_0 plays the role of the so-called template. In the static point-based LDDMM algorithm discussed in the previous section, the time in Eq. (5) is a dummy time only used for algorithmic purposes with the single target observable at $t = 1$, and is not relevant to the time at which the data is collected. In the TS-LDDMM model, the observables, I_t, are generated from I_0 under space-time flows, ϕ_t such that $\phi_t \cdot I_0 = I_t$ at all time t. We define an inexact point-based TS-LDDMM matching: find a time-dependent diffeomorphism ϕ_t connecting a point set $\boldsymbol{x} = I_0 = (x_i)_{i=1}^n$ and time-dependent point sets $\boldsymbol{y}_t = I_t = (y_j(t))_{j=1}^m$ as a minimizer of

$$J(\alpha_t) = \underset{\alpha_t}{\operatorname{argmin}} \int_0^1 \sum_{i=1}^{n} \sum_{j=1}^{n} \left[k_V(x_i(t), x_j(t))\alpha_i(t)\right] \cdot \alpha_j(t) dt + \int_0^1 E_t(\phi_t \cdot x, y_t) dt, \tag{11}$$

where the matching functional, E_t, quantifies the closeness between the deformed template, $\phi_t \cdot \boldsymbol{x}$, and observation, y_t at time t. In our applications, we choose E_t dependent of time and given by Eq. (7) adapted to the unlabeled landmarks, curve, and surface cases.We can rewrite J into a matrix form

$$J(\alpha_t) = \int_0^1 \alpha_t \cdot [k_V(\boldsymbol{x}_t, \boldsymbol{x}_t)\alpha_t] dt + \int_0^1 E_t(\boldsymbol{x}_t, \boldsymbol{y}_t) dt, \tag{12}$$

where $\boldsymbol{\alpha_t} = (\alpha_i(t))_{i=1}^n$, $\boldsymbol{x}_t = \phi_1 \cdot \boldsymbol{x}$, and $\boldsymbol{y}_t = (y_i(t))_{i=1}^n$ are vectors of momentum and coordinates of $\boldsymbol{x}_t$ and $\boldsymbol{y}_t$ at time t.

Lemma 2. *Time-sequence variational solution.* The Euler–Lagrange equation associated with the variational problem in Eq. (12) is given by $(\nabla J)_t = 2\boldsymbol{\alpha}_t + \boldsymbol{\eta}_t = 0$, where vector $\eta_t = \int_t^1 \nabla_{\boldsymbol{x}_s} E_s ds + \int_t^1 (\partial_{\boldsymbol{x}_s} [k_V(x_s, x_s)\alpha_s])^* (\eta_s + \alpha_s) ds$ and $\nabla_{\boldsymbol{x}_s} E_s$ is the derivative of E_s with respect to $\boldsymbol{x}_s$.

The Euler–Lagrange optimality conditions for the point-based TS-LDDMM in Eq. (12) imply

$$\frac{d\alpha_i(t)}{dt} = -\sum_{j=1}^{n} \alpha_i(t) \cdot \alpha_j(t) \nabla_1 k_V(x_i(t), x_j(t)) + \frac{1}{2} \nabla_{x_i(t)} E_t, \tag{13}$$

where ∇_1 denotes taking derivative of $k_V(x_i(t), x_j(t))$ with respect to its first variable and $\nabla_{x_i(t)} E_t$ is the derivative of E_t with respect to $x_i(t)$.

We give the proof of this lemma in Appendix.

Unlike the static point-based LDDMM with shape variations encoded in the initial momentum based on Eqs. (9) and (10), the dynamic shape motion in the point-based TS-LDDMM also depends on the serial observations. Thus, the time-dependent momentum is needed to characterize the dynamic shape motion (not only the initial momentum). In the point-based TS-LDDMM we term this time-dependent momentum as "deformation signature" that carries the dynamic motion of the serial observations.

The sampled TS-LDDMM

The usual problem in Computational Anatomy involves sampled observables in time of the observed data $I_{t_k} = y_{t_k}, k = 1, \ldots, N$ with $t_0 = 0$, $t_N = 1$. Then the variational problem and its solution becomes a mixture of the static and dynamic solutions, interpolating between time points. Between sample points the geodesic satisfies the Euler-equation and conservation of momentum, with the observables entering at the boundary points t_1, t_2, t_N.

Lemma 3. The optimizing flow connecting the observables $y_{t_k}, k = 1, \ldots, N$ given by

$$J(\alpha_t) = \underset{\alpha_t}{\operatorname{argmin}} \int_0^1 \sum_{i=1}^{n} \sum_{j=1}^{n} \left[k_V(x_i(t), x_j(t))\alpha_j(t)\right] \cdot \alpha_i(t) \boldsymbol{dt} + \sum_{k=1}^{N} E_{t_k}\left(\phi_{t_k} \cdot x, y_{t_k}\right) \tag{14}$$

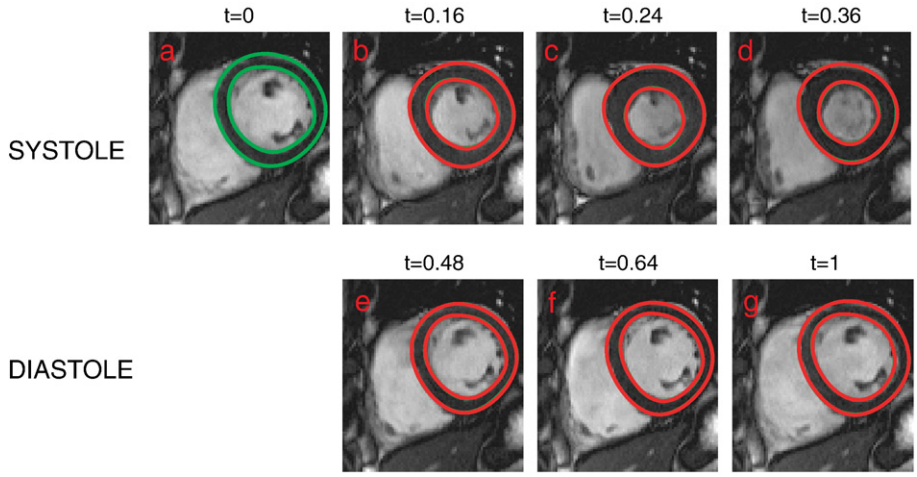

Fig. 2. A coronal section of the left ventricle was selected from the systole phase (panels (a–d)) and the diastole phase (panels (e–g)) during one cardiac cycle. Green curves on each panel are the automatically segmented contours of endocardium and epicardium. Red curves on each panel are the deformed template at each phase. Red and green contours are overlapped very well, which indicates the accuracy of the TS-LDDMM algorithm. The time normalized into the range between 0 and 1 is indicated on the top of each panel.

has Euler–Lagrange optimality conditions for the point-based TS-LDDMM in Eq. (12) given by

$$\frac{d\alpha_i(t)}{dt} = -\sum_{j=1}^{n} \alpha_i(t)\cdot\alpha_j(t)\nabla_1 k_V(x_i(t),x_j(t)), \quad t\in(t_{i-1},t_i), i=1,\ldots,N \tag{15}$$

with jumps at observation times defined as follows: $\alpha_1 = \nabla_{x_1} E_1/2$, and $\alpha_{t_k^+} - \alpha_{t_k^-} = \nabla_{x_{t_k}} E_{t_k}/2$.

We give the proof of this lemma in Appendix (with the expression of the gradient of J with respect to $\boldsymbol{\alpha}$). This situation is intermediate between the static LDDMM and TS-LDDMM. It is easy to check that the whole trajectory $\boldsymbol{\alpha}_t$ is characterized by the momenta at time 0, $\boldsymbol{\alpha}_0$ and at time t_k^+, for $t_k<1$.

Implementation

We use a conjugate gradient routine to perform the minimization of functional J in (11) with respect to variables $\alpha_i(t)$. Of course any other optimization scheme could be considered at this point. The different steps required to compute the functional and its gradient for each iteration are the following:

1. from momentum vectors $\alpha_i(t)$, compute trajectories $x_i(t)$ by integrating the system of ordinary differential equations (ODE) using Eq. (9).
2. evaluate J from Eq. (11)
3. compute vectors $\boldsymbol{\eta}_i(t)$ by integrating the system of ODE in Eq. (21)
4. compute gradient $(\nabla J)_i(t) = 2\alpha_i(t) + \boldsymbol{\eta}_i(t)$.

All time-dependant variables are evaluated on a uniform grid $t_1=0,\ldots, t_T=1$ and a predictor/corrector centered Euler scheme was used to solve the systems of ODE in Eq. (9) and (21). The complexity of each iteration is of order dTN^2, where $N=\max(n, m)$. To speed up computations when N is large, all convolutions by kernels k_V and k_W are accelerated with fast Gaussian transform (Yang et al., 2003), which reduces the complexity to $dTN\log(N)$.

Heart and brain applications

TS-LDDMM of MR heart image

We illustrate an application of the TS-LDDMM for encoding heart motion in cardiac cycles. Total 25 image volumes were acquired per cardiac cycle. For the sake of simplicity, one cardiac cycle from the end-diastole (ED) to the next ED was normalized from $t=0$ to $t=1$ and sampled into 25 time points. Fig. 2 illustrates a coronal section of the left ventricle selected from the systole phase (panels a–d) and the diastole phase (panels e–g). We applied the automatic segmentation algorithm (Jolly, 2006) for contouring the endocardium and epicardium in every phase, which are marked in green curves on each panel. The endocardium and epicardium curves in panel (a) served as template curves in the TS-LDDMM algorithm that map it

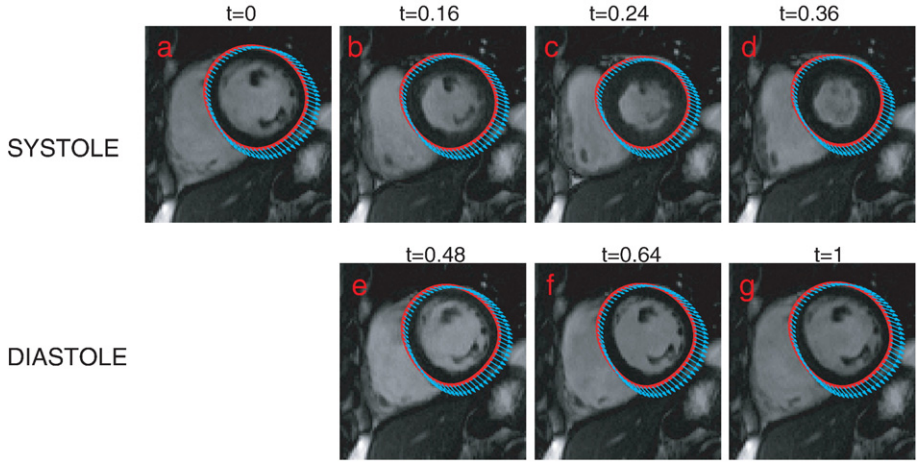

Fig. 3. Momentum vectors, $\boldsymbol{\alpha}_t$, of the epicardium curves computed from the TS-LDDMM algorithm are shown in the template coordinates.

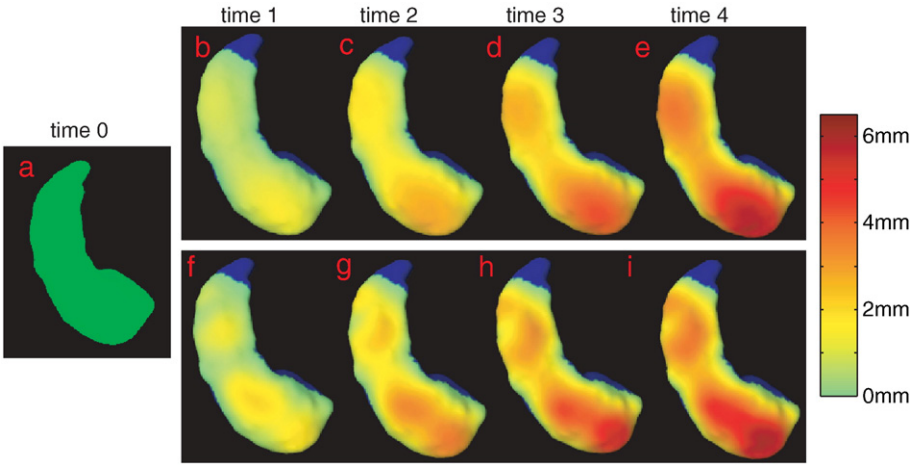

Fig. 4. Panel (a) shows the hippocampal surface at time 0 in the inferior view. Panels (b–e) illustrate the hippocampal surfaces with surface-inward deformation in the subiculum subfield at times 1–4. The strength of the deformation is denoted by its distance to the hippocampal surface at time 0. Panels (f–i) show the deformed template computed from the TS-LDDMM algorithm at each time point. They are colored by their distances to the surface on panel (a). The region with no deformation is colored in blue.

to the curves at the rest of the cardiac cycle. Red curves in Fig. 2 illustrate the deformed templates in each phase of the cardiac cycle, which are well overlapped with the segmented contours. The momentum, $\boldsymbol{\alpha_t}$, of the epicardium curves shown in Fig. 3, encodes the trajectory of the heart motion through the flow in Eq. (9).

TS-LDDMM of hippocampal surface shapes

Subfield-specific shape changes of the hippocampus have been identified in mild cognitive impairment (MCI) and Alzheimer's disease (AD). We demonstrate an application of the TS-LDDMM algorithms for tracking subfield-specific shape changes of the hippocampus in multiple time points in simulated datasets. To do so, we generated two sets of hippocampal surface shapes at five time points: one set with the surface-inward deformation only in the subiculum subfield (Fig. 4); the other with the surface-inward deformation only in the subfields of CA1,2,3 (Fig. 5). In each set, the hippocampal surfaces at time points 1–4 (panels b–e) were generated from the one at time 0 (panel a). Between any two subsequent time points, the reduction in the hippocampal volume is about 10%. Each surface in (panels b–e) is colored by its distance to the surface at time 0 to show the strength of the hippocampal atrophy. In the TS-LDDMM algorithm, each surface was represented by 3223 vertices and 6442 triangles. The hippocampal surface at time 0 was considered as within-subject template and the surfaces at the other time points were considered as time-dependent targets. 20 time steps were chosen between each time interval. The TS-LDDMM mapping for these examples took 7 or 8 min when using a 64-bit computer with a 2.4GHz CPU. Figs. 4 and 5(f–i) show the deformed template computed from the TS-LDDMM algorithm at each time point colored with its distance map to the template at time 0. Visually, the TS-LDDMM algorithm can well map the template to the time-dependent targets through trajectory, ϕ_t.

Making between-subject shape comparison possible requires to translate the deformation signature encoding the within-subject dynamic shape changes (e.g. vectors in Fig. 3) to a global reference frame. In the subsequent section, we describe how the deformation signature obtained from the TS-LDDMM is transported first to the within-subject baseline, then to the global template along the curve connecting the within-subject template with the global template.

Parallel transport in diffeomorphisms

Via relation in Eq. (9) the deformation signature $\boldsymbol{\alpha_t}^{(j)}$ at time t is attached to the current position $\boldsymbol{x}_t^{(j)}$ of the evolving point set for subject j. In this section, we describe how this subject-dependent

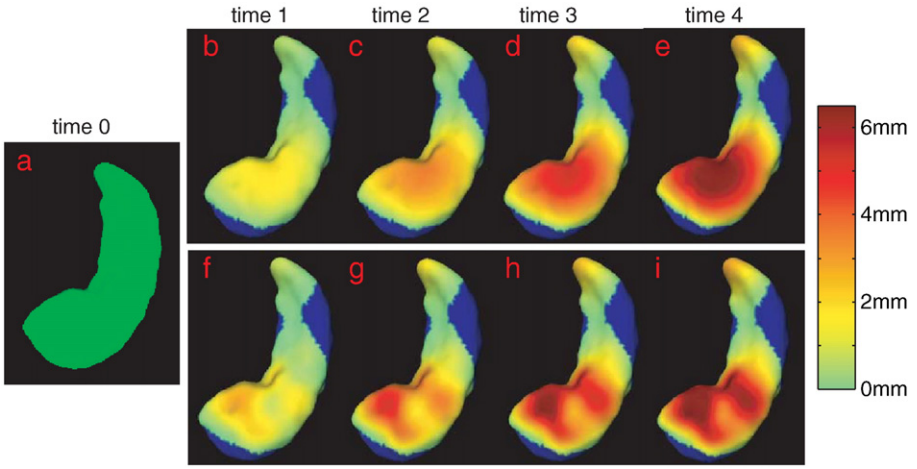

Fig. 5. Panel (a) shows the hippocampal surface at time 0 in the superior view. Panels (b–e) illustrate the hippocampal surfaces with surface-inward deformation in the subfields of CA1, 2, and 3 at times 1–4. The strength of the deformation is denoted by its distance to the hippocampal surface at time 0. Panels (f–i) show the deformed template computed from the TS-LDDMM algorithm at each time point. They are colored by their distances to the surface on panel (a). The region with no deformation is colored in blue.

signature can be normalized to provide a new time series evolving from a fixed (subject independent) baseline, which will be used for the between-subject comparison.

The basic operation for this purpose will be parallel transport in deformable point sets. It is performed along a curve traced on a Riemannian manifold, which allows translation of a tangent vector at one end of the curve to the other end of curve without change according to the intrinsic geometry of the manifold. This has been described in the diffeomorphic matching framework in (Qiu et al., 2008a,b; Younes, 2007; Younes et al., 2008). In the context of this paper, parallel transport takes in input a trajectory, $s \mapsto \mathbf{z}_s$, and a deformation signature $\boldsymbol{\omega}_t$ at some time t (attached to $\mathbf{z}_t$). The output is a transported signature, $\boldsymbol{\omega}_s$, at each time s of the trajectory. They satisfy the following dynamical system

$$\begin{aligned}
&\sum_{j=1}^{n} k_V(z_i(t), z_j(t)) \qquad (16)\\
&\times\left(\frac{d\omega_j(t)}{dt} + \sum_{l=1}^{n} \nabla_1 k_V(z_j(t), z_l(t))\left(\beta_j(t)\cdot\omega_l(t) + \omega_j(t)\cdot\beta_l(t)\right)\right)\\
&= \sum_{j\neq 1}^{n} \nabla_1 k_V(z_i(t), z_j(t))\cdot\left(\left(\sum_{l=1}^{n} k_V(z_i(t), z_l(t))\omega_l(t)\right.\right.\\
&\left.-\sum_{l=1}^{n} k_V(z_j(t), z_l(t))w_l(t)\right)\beta_j(t) - \left(\sum_{l=1}^{n} k_V(z_i(t), z_l(t))\beta_l(t)\right.\\
&\left.\left.-\sum_{l=1}^{n} k_V(z_j(t), z_l(t))\beta_l(t)\right)\omega_j(t)\right),
\end{aligned}$$

where β_t is defined by

$$\frac{dz_i(t)}{dt} = \sum_{j=1}^{n} k_V(z_i(t), z_j(t))\beta_j(t), i = 1, 2, \ldots, n. \qquad (17)$$

Since this is a first order linear dynamical system, knowing $\boldsymbol{\omega}$ at time t uniquely specifies its value at all times.

The following notation will be convenient. Define $PT(\mathbf{z}, t, \tilde{\omega}, s)$ the solution at time s of System (16), for the curve $s \mapsto \mathbf{z}_s$ and $\omega_t = \tilde{\omega}$ at time t (i.e., the parallel translation of $\tilde{\omega}$ along $\mathbf{z}$ from time t to time s). Then, as illustrated in Fig. 1, our normalization procedure for TS-LDDMM deformation signatures is defined as follows. We assume that a global template $\mathbf{x}_0^{(0)}$ has been chosen, as an examplar of the subject baselines, $\mathbf{x}_0^{(j)}$.

Retraction: For each subject j and each time t, parallel translate $\boldsymbol{\alpha}_t^{(j)}$ from time t to time 0 along $s \mapsto \mathbf{x}_s^{(j)}$, yielding a vector denoted $\beta_0^{(j,t)}$. With our notation, this is

$$\beta_0^{(j,t)} = PT\left(\mathbf{x}^{(j)}, t, \alpha_t^{(j)}, 0\right).$$

Translation: For each j, compute a geodesic $\mathbf{z}^{(j)}$ between $\mathbf{x}_0^{(j)}$ and the template $\mathbf{x}_0^{(0)}$ by solving the LDDMM problem in Eq. (5). Then, translate $\beta_0^{(j,t)}$ along this trajectory, yielding $\boldsymbol{\omega}_0^{(j,t)}$. Thus,

$$\omega_0^{(j,t)} = PT\left(\mathbf{z}^{(j)}, 0, \beta_0^{(j,t)}, 1\right).$$

Extension: This is the inverse of the retraction operation. For each j and each t, reconstruct a new trajectory $\mathbf{y}_t^{(j)}$ starting from the global template ($\mathbf{y}_0^{(j)} = \mathbf{x}_0^{(0)}$), solving the system

$$\frac{d\mathbf{y}_t^{(j)}}{dt} = k_v(\mathbf{y}_t, \mathbf{y}_t)\omega_t^{(j,t)}$$

with $\boldsymbol{\omega}_t^{(j,t)} = PT(\mathbf{y}^{(j)}, 0, \boldsymbol{\omega}_0^{(j,t)}, t)$.

The result of this algorithm is a subject-indexed family of trajectories ($\mathbf{y}_t^{(j)}$) which are all deformations of the same template, and therefore can be compared in a meaningful way. The extension step requires a double integration in its implementation: at each time t, parallel translation (Eq. (16)) must be solved from 0 to t in order to update the trajectory $\mathbf{y}_t^{(j)}$.

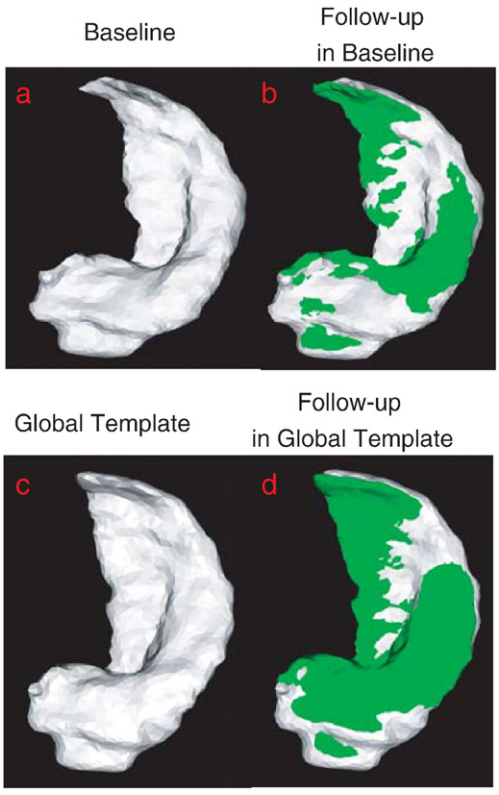

Fig. 6. Panel (a) shows the hippocampus of a subject at the baseline. The hippocampus surface of this subject at the follow-up (green) is superimposed with one at the baseline in panel (b). Panel (c) shows the global hippocampus template. Panel (d) shows the hippocampus of this subject at the follow-up (green) represented in the global template coordinates (gray).

Fig. 6 intuitively illustrates one example using parallel transport to represent within-subject deformation in the global template coordinates. Panel (a) shows the hippocampal surface of a subject at the baseline while Panel (b) shows the hippocampal surface of the same subject at the follow-up (green) superimposed with one at the baseline (gray). Panel (c) depicts the global hippocampal template. Panel (d) shows the hippocampal surface of this subject at the follow-up (green) represented in the global template coordinates (gray). The deformation of the hippocampal surface between baseline and follow-up represented by interlacing green and gray in panel (b) has a similar pattern as in panel (d). This indicates that the technique of parallel transport in diffeomorphism is a reasonable approach allowing us to study longitudinal shape variation within subjects in a global template coordinate system.

TS-LDDMM and parallel transport for hippocampal atrophy

We applied the TS-LDDMM and parallel transport algorithms for assessing differences in the hippocampal shape changes between 19 healthy elders (age: 74.6±6.5) and 19 patients with Alzheimer's disease (AD) (age: 74.0±6.8). Each subject was scanned every three months so there were four MRI volumes per subject in a nine-month interval.

In structural delineation process, the hippocampus of each subject at the baseline was semi-automatically segmented using the method described in (Haller et al., 1997) and was then propagated to the rest time points using the LDDMM-image mapping (Beg et al., 2005). We represented the hippocampal shape using triangulated meshes. In the mapping process, the TS-LDDMM algorithm was applied to find an

optimal trajectory that passes through the four observations of each subject in a metric shape space. This trajectory and its corresponding momenta encode the within-subject time-dependent shape changes. Then, following the illustration in Fig. 1, the parallel transport operation first translated the within-subject time dependent momenta to the subject's baseline coordinate system, and then to the global template. The within-subject shape trajectory was reconstructed in the global template coordinates via the flow and parallel transport. Finally, we computed the Jacobian matrix of the within-subject deformation in the global template $x^{(0)}$, through the flow equation in Eq. (9) when $\boldsymbol{\alpha}_t = \boldsymbol{\omega}_t^{(j,\,t)}$. The Jacobian determinant shows regions with expansion (Jacobian>1) or compression (Jacobian<1). Let $F^{(j)}(p)$, $p \in x^{(0)}$ denote the Jacobian determinant in the logarithmic scale for subject j.

To illustrate our results, we performed the statistical testing on the log Jacobian determinant that characterizes the shape changes in nine months. Assume $F^{(j)}(x)$ arises from random processes. Its distribution models as random field in the global template that can be represented by a linear combination of orthonormal bases as follows:

$$F^{(j)}(x) = \sum_{i=1}^{10} F_i^{(j)} \psi_i(x), \quad x \in \boldsymbol{x}^{(0)}, \tag{18}$$

where $\psi_i(x)$ is chosen as the ith basis of the Laplace–Beltrami (LB) operator on $x^{(0)}$ (Qiu et al., 2006). $F_i^{(j)}$ is the coefficient associated with ψ_i. In our study, 10 LB bases take 90% of total variation of $F^{(j)}$. We hypothesized that the $F_i^{(j)}$s are equal in the groups of healthy elders and patients with AD against that the $F_i^{(j)}$s are not equal in both groups. To examine it, we performed two-sided Student t-tests on each individual $F_i^{(j)}$. At a significance level of 0.02, the shape differences between the two groups occur in the 1st (p=0.0171) and the 4th (p=0.0159) LB bases of the left hippocampus and the 3rd (p=0.0032) and the 10th p=0.0156 LB bases of the right hippocampus. For the visualization purpose, we back projected these LB bases to the global template coordinates, which is shown in both superior and inferior views of the hippocampus in Fig. 7. Compared with the healthy controls, regions in warm color have greater atrophy in patients with AD, while regions in cool color have less atrophy. This result suggests that the greater atrophy occurs in the left hippocampus, particularly in the posterior segment, and the lateral middle body of the right hippocampus.

Discussion

This paper presents shape analysis algorithms for tracking longitudinal shape changes for point-based objects, including unlabeled landmarks, curves, and surfaces, under the diffeomorphic mapping framework. It incorporates two major diffeomorphic techniques: TS-LDDMM and parallel transport. The dynamic motion or shape change is encoded via time-dependent momentum obtained from TS-LDDMM. The parallel transport operation taken from Riemannian geometry in a diffeomorphic shape space translates these momentum vectors (tangent vectors) in the shape space to within-subject baseline coordinates and then to the global template without incorporating across-subject deformation. It preserves the metric or covariance of the momentum from a subject coordinate system to the global template coordinate system. The benefit from it is to directly make statistical inference for detecting across-subject shape differences.

The TS-LDDMM algorithms introduced in this paper are the extension of the static point-based LDDMM algorithms (Glaunès et al., 2004, 2008; Vaillant and Glaunès, 2005; Vaillant et al., 2007; Qiu and Miller, 2007). We consider point-based shapes, such as unlabeled landmarks, curves, and surfaces, as measure. The structure of a Hilbert space is imposed on the measure in the way its norm can be used to quantify the geometric similarity between two objects (Glaunès et al., 2008; Vaillant and Glaunès, 2005). We generalized the gradient derivation of the energy in the TS-LDDMM variational problem with respect to the momentum along the deformation trajectory for the point-based shapes, including unlabeled points, curves, and surfaces. Unlike the static LDDMM encoding the shape variation in the initial momentum, the TS-LDDMM Euler–Lagrange optimality conditions indicate that time-dependent shape changes are characterized by the time-dependent momentum, which do not satisfy the geometric evolution of Eqs. (9) and (10). The TS-LDDMM algorithm provides a way to fit subject's time-dependent observations by a smooth trajectory in the metric space.

The demonstration of the use of the TS-LDDMM and parallel transport is given through an example of detecting time-dependent hippocampal atrophy pattern in AD. A variety of other applications using the proposed analysis framework can be found in medical image analysis and computer vision (e.g. studying heart motion abnormalities in cardiac diseases).

Role of the funding source

National University of Singapore start-up grant R-397-000-058-133 and A*STAR SERC 082-101-0025 provided financial support for the conduct of the research.

Conflict of interest

The authors declare that there are no conflicts of interest.

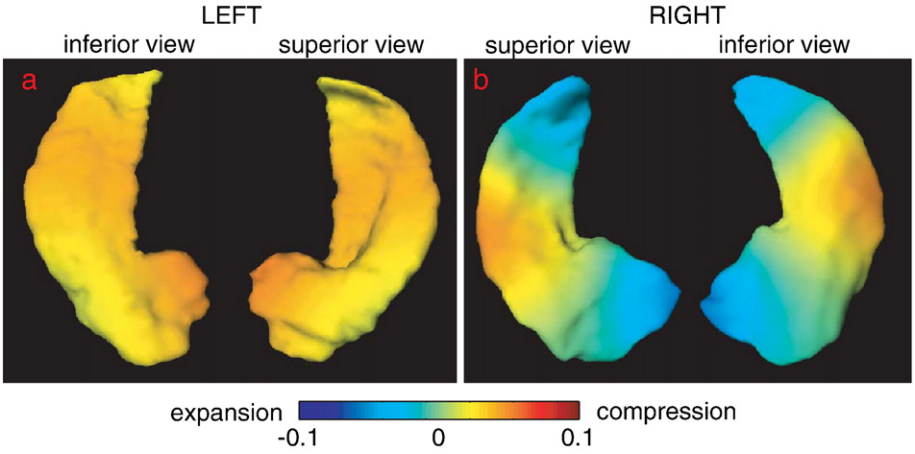

Fig. 7. Panel (a) shows the shape differences of the left hippocampus between the healthy elders and patients with AD in boths superior and inferior views. Panel (b) illustrates the shape differences of the right hippocampus. Compared with the healthy elders, regions with greater atrophy in the AD group are in warm color and regions with less atrophy in the AD group are in cool color.

Acknowledgements

The work reported here was supported by National University of Singapore start-up grant R-397-000-058-133 and A*STAR SERC 082-101-0025. The author would like to thank Dr Martin Hadamitzky at Deutsches Herzzentrum, Germany and Dr. Ying Sun at National University of Singapore for providing the cardiac MRI data and the segmented contours of the endocardium and epicardium.

Appendix A. Gradient of a point-based matching functional in the TS-LDDMM setting

Lemma 4. The Euler–Lagrange equation associated with the variational problem in Eq. (12) is given by $(\nabla J)_t = 2\alpha_t + \eta_t = 0$, where vector $\eta_{lt} = \int_t^1 \nabla_{x_s} E_s ds + \int_t^1 (\partial_{x_s}[k_V(\boldsymbol{x}_s, \boldsymbol{x}_s)\alpha_s])^*(\eta_s + \alpha_s) ds$ and $\nabla_{x_s} E_s$ is the derivation of E_s with respect to $\boldsymbol{x}_s$.

Proof. We consider a variation $\boldsymbol{\alpha}_t^\epsilon = \boldsymbol{\alpha}_t + \epsilon\tilde{\boldsymbol{\alpha}}_t$. Our goal is to express the derivative $f'(0)$ of $f(\epsilon) \doteq J(\alpha_t^\epsilon)$ in function of $\tilde{\boldsymbol{\alpha}}_t$.

Since

$$\frac{d\boldsymbol{x}_t}{dt} = k_V(\boldsymbol{x}_t, \boldsymbol{x}_t)\alpha_t.$$

The variation in $\boldsymbol{\alpha}$ implies a first order variation in $\boldsymbol{x}$, that we denote $\tilde{\boldsymbol{x}}$ with

$$\frac{d\tilde{x}_t}{dt} = \partial_x(k_V(\boldsymbol{x}_t, \boldsymbol{x}_t)\alpha_t)\tilde{x}_t + k_V(\boldsymbol{x}_t, \boldsymbol{x}_t)\tilde{\alpha}_t.$$

From

$$J(\alpha) = \int_0^1 \alpha_t \cdot (k_V(\boldsymbol{x}_t, \boldsymbol{x}_t)\alpha_t) dt + \int_0^1 E_t(\boldsymbol{x}_t, \boldsymbol{y}_t) dt$$

we get

$$f'(0) = 2\int_0^1 \alpha_t \cdot (k_V(\boldsymbol{x}_t, \boldsymbol{x}_t)\alpha_t) dt + \int_0^1 (\nabla_{\boldsymbol{x}_t}(\alpha_t \cdot k_V(\boldsymbol{x}_t, \boldsymbol{x}_t)\alpha_t) + \nabla_{\boldsymbol{x}} E_t(x_t)) \cdot \tilde{\boldsymbol{x}}_t dt. \tag{19}$$

Introduce the matrix $\mathbf{R}_{st}$ defined by $\mathbf{R}_{ss}$ = identity and

$$\frac{d\mathbf{R}_{st}}{dt} = \partial_{x_t}[k_V(\boldsymbol{x}_t, \boldsymbol{x}_t)\alpha_t]\mathbf{R}_{st}.$$

Then we have

$$\tilde{\boldsymbol{x}}_t = \int_0^t \mathbf{R}_{st} k_V(\boldsymbol{x}_s, \boldsymbol{x}_s)\tilde{\alpha}_s ds,$$

as can be easily checked. Also, $\mathbf{R}_{st}\mathbf{R}_{ts}$ = identity which implies

$$\frac{d\mathbf{R}_{st}^*}{ds} = -\partial_{x_t}[k_V(\boldsymbol{x}_t, \boldsymbol{x}_t)\alpha_t]^* \mathbf{R}_{st}^*.$$

Introducing

$$\eta_{lt} = \int_t^1 \mathbf{R}_{ts}^*(\nabla_{\boldsymbol{x}_s}(\alpha_s \cdot k_V(\boldsymbol{x}_s, \boldsymbol{x}_s)\alpha_s) + \nabla_{\boldsymbol{x}} E_s(\boldsymbol{x}_s)) ds,$$

we can rewrite Eq. (19) as

$$f'(0) = 2\int_0^1 \alpha_t \cdot (k_V(\boldsymbol{x}_t, \boldsymbol{x}_t)\alpha_t) dt + \int_0^1 \eta_t \cdot (k_V(\boldsymbol{x}_t, \boldsymbol{x}_t)\alpha_t) dt \tag{20}$$

with $\eta_1 = 0$ and

$$\frac{d\eta_{lt}}{dt} = -\nabla_{\boldsymbol{x}_t} E_t(\boldsymbol{x}_t) - \partial_{\boldsymbol{x}_t}[k_V(\boldsymbol{x}_t, \boldsymbol{x}_t)\alpha_t]^*(\alpha_t + \eta_t) \tag{21}$$

where we have used the fact that

$$\nabla_{\boldsymbol{x}_t}\left(\alpha_t \cdot k_V(\boldsymbol{x}_t, \boldsymbol{x}_t)\right)\alpha_t = \partial_{\boldsymbol{x}_t}[k_V(\boldsymbol{x}_t, \boldsymbol{x}_t)\alpha_t]^*\alpha_t.$$

This provides the Euler Lagrange equations stated in the lemma. Moreover, from $2\boldsymbol{\alpha}_t = -\eta_{lt}$ we get

$$\frac{d\alpha_t}{dt} = \frac{1}{2}\nabla_{\boldsymbol{x}_t} E_t(\boldsymbol{x}_t) - \frac{1}{2}\partial_{\boldsymbol{x}_t}[k_V(\boldsymbol{x}_t, \boldsymbol{x}_t)\alpha_t]^*(\alpha_t)$$

which coincide with the expression given in Lemma 2. This result was detailed in Glaunès et al. (2004) for unlabeled landmarks, Glaunès et al. (2008) for curves, and Vaillant and Glaunès (2005) for surfaces.

The proof of Lemma 3 is very similar. We leave the details of the computation to the reader. One finds that the gradient of J is given by $2\boldsymbol{\alpha}_t + \boldsymbol{\eta}_t$ with

$$\eta_{lt} = \int_t^1 \mathbf{R}_{ts}^*(\partial_{x_s}(k_V(\boldsymbol{x}_s, \boldsymbol{x}_s)\alpha_s)) ds + \sum_k \mathbf{R}_{tt_k}^* \nabla_{\boldsymbol{x}_{t_k}} E_{t_k} 1_{[t_k,1]}(t).$$

Computing the derivative as above, one finds that at all $t \neq t_k$, $d\eta_{lt}$ satisfies

$$\frac{d\eta_{lt}}{dt} = -\partial_{\boldsymbol{x}_t}[k_V(\boldsymbol{x}_t, \boldsymbol{x}_t)\alpha_t]^*(\alpha_t + \eta_{lt});$$

$\boldsymbol{\eta}_t$ is discontinuous at observation times with $\eta_1 = \nabla_{\boldsymbol{x}_1} E_1$, and the jump $\eta_{lt_k^-} - \eta_{lt_k^+} = \nabla_{\boldsymbol{x}_{t_k}} E_{t_k}$. This translates directly into the conditions given in Lemma 3.

We have implicitly defined the gradient of J relatively to the metric given by $k_V(\mathbf{x}_t, \mathbf{x}_t)$ with two-fold advantages of being closer to the metric inducing the space of velocity field v_t and simplifying the formula for the gradient.

References

Apostolova, L.G., Dinov, I.D., Dutton, R.A., Hayashi, K.M., Toga, A.W., Cummings, J.L., Thompson, P.M., 2006a. 3D comparison of hippocampal atrophy in amnestic mild cognitive impairment and Alzheimer's disease. Brain 129, 2867–2873.

Apostolova, L.G., Dutton, R.A., Dinov, I.D., Hayashi, K.M., Toga, A.W., Cummings, J.L., Thompson, P.M., 2006b. Conversion of mild cognitive impairment to Alzheimer disease predicted by hippocampal atrophy maps. Arch. Neurol. 63, 693–699.

Ashburner, J., 2007. A fast diffeomorphic image registration algorithm. Neuroimage 38 (1), 95–113.

Ashburner, J., Friston, K.J., 2005. Unified segmentation. NeuroImage 26, 839–851.

Ashburner, J., Csernansky, J.G., Davatzikos, C., Fox, N.C., Frisoni, G.B., Thompson, P.M., 2003. Computer-assisted imaging to assess brain structure in healthy and diseased brains. Lancet Neurology 2, 79–88.

Avants, B., Gee, J.C., 2004. Geodesic estimation for large deformation anatomical shape and intensity averaging. NeuroImage 23, 139–150.

Avants, B.B., Schoenemann, P.T., Gee, J.C., 2006. Lagrangian frame diffeomorphic image registration: morphometric comparison of human and chimpanzee cortex. Med. Image Anal. 10, 397–412.

Bajcsy, R., Kovacic, S., 1989. Multiresolution elastic matching. Comput. Vis. Graph. Image Process. 46, 1–21.

Bajcsy, R., Lieberson, R., Reivich, M., 1983. A computerized system for the elastic matching of deformed radiographic images to idealized atlas images. J. Comp. Assist. Tomog. 7, 618–625.

Bakker, A., Kirwan, C., Miller, M., Stark, C., 2008. Pattern separation in the human hippocampal ca3 and dentate gyrus. Science 319, 1640–1642.

Beg, M.F., Miller, M.I., Trouvé, A., Younes, L., 2005. Computing large deformation metric mappings via geodesic flows of diffeomorphisms. Int. J. Comput. Vis. 61, 139–157.

Bookstein, F.L., 1978. The Measurement of Biological Shape and Shape Change, Vol. 24. Springer-Verlag: Lecture Notes in Biomathematics, New York.

Bookstein, F., 1991. Morphometric Tools for Landmark Data. Cambridge University Press, New York.

Bookstein, F.L., 1996. Landmark methods for forms without landmarks: morphometrics of group differences in outline shape. Med. Image Anal. 1, 225–243.

Bookstein, F.L., 1997. Shape and the information in medical images: a decade of the morphometric synthesis. Comput. Vis. Graph. Image Process. 66, 97118.

Brambati, S.M., Renda, N.C., Rankin, K.P., Rosen, H.J., Seeley, W.W., Ashburner, J., Weiner, M.W., Miller, B.L., Gorno-Tempini, M.L., 2007. A tensor based morphometry study of longitudinal gray matter contraction in ftd. Neuroimage 35, 998–1003.

Cachier, P., Mangin, J.-F., Pennec, X., Rivière, D., Papadopoulos-Orfanos, D., Régis, J., Ayache, N., 2001. Multisubject non-rigid registration of brain MRI using intensity and geometric features. MICCAI '01: Proceedings of the 4th International

Conference on Medical Image Computing and Computer-Assisted Intervention. Springer-Verlag, London, UK, pp. 734–742.
Cao, Y., Miller, M., Winslow, R., Younes, L., 2005a. Large deformation diffeomorphic metric mapping of vector fields. IEEE Trans. Med. Imag. 24, 1216–1230.
Cao, Y., Miller, M.I., Winslow, R.L., Younes, L., 2005b. Large deformation diffeomorphic metric mapping of fiber orientations. ICCV. IEEE Computer Society, Beijing, China, pp. 1379–1386.
Christensen, G.E., Joshi, S.C., Miller, M.I., 1997. Volumetric transformation of brain anatomy. IEEE Trans. Medical Imaging 16, 864–877.
Chung, M.K. 2001, Statistical morphometry in neuroanatomy, Ph. D thesis, Department of Mathematics and Statistics, McGill University, Montreal.
Chung, M., Worsley, K., S., R., Paus, T., Taylor, J., Giedd, J., Rapoport, J., A.C., E., 2001. Statistical analysis of cortical surface area change, with an application to brain growth. Neuroimage 13, S96.
Chung, M., Dalton, K., Davidson, R., 2008. Tensor-based cortical surface morphometry via weighed spherical harmonic representation. IEEE Trans. Med. Imag 27 (8), 1143–1151.
Collins, D.L., Neelin, P., Peters, T.M., Evans, A.C., 1994. Automatic 3D intersubject registration of MR volumetric data in standardized Talairach space. J. Comp. Assist. Tomog. 18, 192–205.
Collins, D.L., Goualher, G.L., Evans, A.C., 1998. Non-linear cerebral registration with sulcal constraints. MICCAI '98: Proceedings of the First International Conference on Medical Image Computing and Computer-Assisted Intervention. Springer-Verlag, London, UK, pp. 974–984.
Csernansky, J.G., Schindler, M.K., Spliner, N.R., Wang, L., Gado, M., Selemon, L.D., Rastogi-Cruz, D., Posener, P.A., Miller, M.I., 2004. Abnormalities of thalamic volume and shape in schizophrenia. Am. J. Psychiatr. 161, 896–902.
Dann, R., Hoford, J., Kovacic, S., Reivich, M., Bajcsy, R., 1989. Evaluation of elastic matching systems for anatomic (CT, MR) and functional (PET) cerebral images. J. Comp. Assist. Tomog. 13, 603–611.
Davatzikos, C., 1996. Spatial normalization of 3-d brain images using deformable models. J. Comp. Assist. Tomog. 20, 656–665.
Dupuis, P., Grenander, U., Miller, M.I., 1998. Variational problems on flows of diffeomorphisms for image matching. Quaterly of Applied Math. 56, 587–600.
Durrleman, S., Pennec, X., Trouvé, A., Ayache, N., 2007. Measuring brain variability via sulcal lines registration: a diffeomorphic approach. MICCAI (1), pp. 675–682.
Feldmar, J., Ayache, N., Betting, F., 1997. 3D–2D projective registration of free-form curves and surfaces. Comput. Vis. Graph. Image Process.: CVIU 65, 403–424.
Fischl, B., Sereno, M.I., Dale, A.M., 1999. Cortical surface-based analysis II: inflation, flattening, and a surface-based coordinate system. NeuroImage 9, 195–207.
Friston, K., Ashburner, J., Frith, C., Poline, J.-B., Heather, J.D., Frackowiak R. SR., 1995. Spatial registration and normalization of images. Hum. Brain Mapp. 2, 165–189.
Gee, J.C., 1999. On matching brain volumes. Pattern Recognition 32, 99–111.
Gee, J., Haynor, D., 1999. Numerical methods for high-dimensional warps. In: Toga, A.W. (Ed.), Brain Warping. Academic Press, San Diego, CA, pp. 101–113.
Gilmore, J., Lin, W., Prastawa, M., Looney, C., Vetsa, Y., Knickmeyer, R., Evans, D., Smith, J., Hamer, R., Lieberman, J., Gerig, G., 2007. Regional gray matter growth, sexual dimorphism, and cerebral asymmetry in the neonatal brain. J. Neurosci. 27, 1255–1260.
Glaunès, J., Trouvé, A., and Younes, L. 2004. Diffeomorphic matching of distributions: a new approach for unlabelled point-sets and sub-manifolds matching, in IEEE Computer Society: Computer Vision and Pattern Recognition, Washington, DC, pp. 712–718.
Glaunès, J., Qiu, A., Miller, M.I., Younes, L., 2008. Large deformation diffeomorphic metric curve mapping. Int. J. Comput. Vis. 80 (3), 317–336.
Haller, J.W., Banerjee, A., Christensen, G.E., Gado, M., Joshi, S., Miller, M.I., Sheline, Y., Vannier, M.W., Csernansky, J.G., 1997. Three-dimensional hippocampal MR morphometry with high-dimensional transformation of a neuroanatomic atlas. Radiology 202, 504–510.
Hellier, P., Barillot, C., 2003. Coupling dense and landmark-based approaches for nonrigid registration. IEEE Trans. Med. Imag. 22, 217–227.
Jolly, M.-P., 2006. Automatic segmentation of the left ventricle in cardiac MR and CT images. Int. J. Comput. Vis. 70, 151–163.
Joshi, S.C., Miller, M.I., 2000. Landmark matching via large deformation diffeomorphisms. IEEE Trans. Image Processing 9, 1357–1370.
Kipps, C.M., Duggins, A.J., Mahant, N., Gomes, L., Ashburner, J., McCusker, E.A., 2005. Progression of structural neuropathology in preclinical Huntington's disease: a tensor based morphometry study. J. Neurol. Neurosurg. Psychiatry 76, 650–655.
Kirwan, C.B., Jones, C., Miller, M.I., Stark, C.E., 2007. High-resolution fMRI investigation of the medial temporal lobe. Hum. Brain Mapp. 28, 959–966.
Mangin, J.-F., Riviere, D., Cachia, A., Duchesnay, E., Cointepas, Y., Papadopoulus-Orfanos, D., Ochiai, T., Regis, J., 2004. A framework for studying cortical folding patterns. NeuroImage 23, S129–S138.
Miller, M.I., Trouvé, A., Younes, L., 2002. On metrics and Euler–Lagrange equations of computational anatomy. Ann. Rev. Biomed. Engng. 4, 375–405.
Miller, M.I., Beg, M.F., Ceritoglu, C., Stark, C., 2005. Increasing the power of functional maps of the medial temporal lobe by using large deformation diffeomorphic metric mapping. Proc. Natl. Acad. Sci. 102, 9685–9690.
Miller, M.I., Trouvé, A., Younes, L., 2006. Geodesic shooting for computational anatomy. J. Math. Imaging Vis. 24, 209–228.
Qiu, A., Miller, M.I., 2007. Cortical hemisphere registration via large deformation diffeomorphic metric curve mapping. The 10th International Conference on Medical Image Computing and Computer Assisted Intervention, Vol. 10, pp. 186–193.
Qiu, A., Miller, M.I., 2008. Multi-structure network shape analysis via normal surface momentum maps. NeuroImage 42 (4), 1430–1438.
Qiu, A., Bitouk, D., Miller, M.I., 2006. Smooth functional and structural maps on the neocortex via orthonormal bases of the Laplace–Beltrami operator. IEEE Trans. Med. Imaging 25, 1296–1306.
Qiu, A., Younes, L., Wang, L., Ratnanather, J.T., Gillepsie, S.K., Kaplan, G., Csernansky, J.G., Miller, M.I., 2007. Combining anatomical manifold information via diffeomorphic metric mappings for studying cortical thinning of the cingulate gyrus in schizophrenia. Neuroimage 37, 821–833.
Qiu, A., Younes, L., Miller, M.I., 2008a. Intrinsic and extrinsic analysis in computational anatomy. Neuroimage 39, 1803–1814.
Qiu, A., Younes, L., Miller, M.I., Csernansky, J.G., 2008b. Parallel transport in diffeomorphisms distinguishes the time-dependent pattern of hippocampal surface deformation due to healthy aging and the dementia of the Alzheimer's type. NeuroImage 40, 68–76.
Rao, A., Chandrashekara, R., Sanchez-Ortiz, G.I., Mohiaddin, R., Aljabar, P., Hajnal, J.V., Puri, B.K., Rueckert, D., 2004. Spatial transformation of motion and deformation fields using nonrigid registration. IEEE Trans. Med. Imaging 23, 1065–1076.
Terriberry, T.B., Joshi, S.C., Gerig, G., 2005. Hypothesis testing with nonlinear shape models. Inf. Process Med. Imaging 19, 15–26.
Thirion, J., 1998. Image matching as a diffusion process: an analogy with Maxwell's demons. Med. Image Anal. 2, 243260.
Thompson, P.M., Schwartz, C., Lin, R.T., Khan, A.A., Toga, A.W., 1996a. Three-dimensional statistical analysis of sulcal variability in the human brain. J. Neurosci. 16, 4261–4274.
Thompson, P.M., Schwartz, C., Toga, A.W., 1996b. High-resolution random mesh algorithms for creating a probabilistic 3D surface atlas of the human brain. NeuroImage 3, 19–34.
Thompson, P.M., Giedd, J.N., Woods, R.P., MacDonald, D., Evans, A.C., Toga, A.W., 2000. Growth patterns in the developing brain detected by using continuum mechanical tensor maps. Nature 404, 190–193.
Trouvé, A. 1995. An infinite dimensional group approach for physics based models, Technical report (electronically available at http://www.cis.jhu.edu) (Unpublished).
Vaillant, M., Glaunès, J., 2005. Surface matching via currents. Lecture Notes in Comp. Sci.: Inform. Proc. in Med. Imaging 3565, 381–392.
Vaillant, M., Miller, M.I., Younes, L., Trouvé, A., 2004. Statistics on diffeomorphisms via tangent space representations. NeuroImage 23, 161–169.
Vaillant, M., Qiu, A., Glaunès, J., Miller, M.I., 2007. Diffeomorphic metric surface mapping in subregion of the superior temporal gyrus. NeuroImage 34, 1149–1159.
van Essen, D., 2004. Surface-based approaches to spatial localization and registration in primate cerebral cortex. NeuroImage 23, s97–s107.
Wang, L., Swank, J.S., Glick, I.E., Gado, M.H., Miller, M.I., Morris, J.C., Csernansky, J.G., 2003. Changes in hippocampal volume and shape across time distinguish dementia of the alzheimer type from healthy aging*. NeuroImage 20, 667–682.
Xue, H., Srinivasan, L., Jiang, S., Rutherford, M.A., Edwards, A.D., Rueckert, D., Hajnal, J.V., 2007. Longitudinal cortical registration for developing neonates. MICCAI (2), pp. 127–135.
Yang, C., Duraiswami, R., Gumerov, N., Davis, L., 2003. Improved fast gauss transform and efficient kernel density estimation. IEEE International Conference on Computer Vision, pp. 464–471.
Younes, L., 2007. Jacobi fields in groups of diffeomorphisms and applications. Q. Appl. Math. 65, 113–134.
Younes, L., Qiu, A., Winslow, R.L., Miller, M.I., 2008. Transport of relational structures in groups of diffeomorphisms. J. Math. Imaging Vis. 32 (1), 41–56.
Yu, P., Grant, P., Qi, Y., Han, X., Sgonne, F., Pienaar, R., Busa, E., Pacheco, J., Makris, N., Buckner, R.L., Golland, P., Fischl, B., 2007. Cortical surface shape analysis based on spherical wavelets. IEEE Trans. Med. Imaging 26, 582–597.